Two-photon interference on Young's double slit

Jelmer Renema
Master project
June-December 2007

June 16, 2008

Contents

List of Figures

1 Introduction

The double-slit experiment has been used to elucidate the principles of quantum mechanics since the Bohr-Einstein debates of the 1920s and 1930s [1]. The central concept in this experiment is *complementarity*, the fact that which-path information at the double slit washes out the interference pattern at the detection screen. This concept is intimately related to the wave-particle duality.

In 1995, Jaeger, Shimony and Vaidman introduced a second complementarity relation for a double slit system, that of complementarity between the visibility of one- and two-photon interference fringes [2]. The first experiments on two-photon interference behind a double slit were performed by Hong and Noh [3] and Fonseca *et al* [5]. Complementarity was first experimentally demonstrated by Abouraddy *et al* [4], albeit over a limited range.

This report presents the results of an experimental study into complementarity between one- and two-photon interference on a double slit system, performed with photon pairs generated by a SPDC source. The experiments have been performed with an unprecedentedly high signal-to-noise ratio. Furthermore, we have probed new areas of the parameter space, and extended the analysis of the experiment to these areas.

In the chapter 2 of this report, a broad outline of the experiment is given. In the third chapter, the theory of this experiment will be treated, with emphasis on how complementarity arises naturally from the visibility of the interference patterns. An interpretation of the experiment in terms of Bell states will also be given. In the fourth chapter, the setup will be described. In the last two chapters, the results from the experiment will be presented and analyzed.

2 Outline

The first demonstration of two-photon interference behind a double slit was performed by Fonseca *et al* in 1998 [5]. In this experiment a system of two slits cut in an opaque screen is illuminated by pairs of photons generated by spontaneous parametric down-conversion (SPDC).

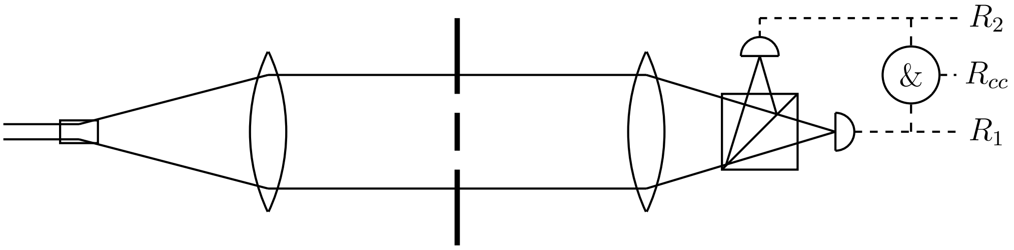

Figure 1: The measured signals in two-photon interference.

In such an experiment interference fringes can be observed both in the uncorrelated count rates R_1 and R_2 of individual photons, and in the coincidence count rate R_{cc} of photon pairs. However, due to complementarity between the spatial entanglement of a pair of photons and the coherence of the members of the pair, an increase in the visibility of the two-photon interference pattern leads to a decrease in the visibility of the one-photon interference-pattern and vice versa.

In a later experiment by Abouraddy *et al* [4], this complementarity between one- and two-photon interference was experimentally demonstrated for the first time.

However, these early experiments suffered from low signal strength. Two reasons may be given for this: first of all the lack of high-brightness sources of photon pairs, and secondly losses due to the optical design of the experimental setup. This later issue was addressed by Hong and Noh [3], who used cylinder lenses to optimize light collection in their version of the experiment.

The experiments described in this master's thesis are a highly improved study of two-photon interference behind Young's double slit. We have implemented several innovations. First of all, due to the use of a periodically poled $KTiOPO_4$ (PPKTP) nonlinear crystal, it becomes possible to achieve signal strengths up to 1000 times higher than those of earlier experiments. Secondly, we will perform the experiment both with near-field illumination of the double slit by the crystal, and with far-field illumination. We will also consider the intermediate case of defocused near-field illumination. In contrast to earlier experiment, we will use an $f - f$ system to achieve far-field illumination, instead of propagation over a sufficiently large distance. The advantage of this is that in our configuration, wavefront curvature is absent.

The analysis of the experiment will be made in terms of a measure of visibility which can be defined on the two-photon count rate as function of the position of two detectors. We will also present an analysis in terms of Bell states of the spatial degrees of freedom of a photon pair.

3 Theory

3.1 Complementarity curve

Consider a double slit that is illuminated by pairs of photons, which have a transverse coherence width much larger than the slit width. Ignoring the field structure along the y-axis, the slits may be treated as point sources and the two photon field behind the slits can be written as

$$|\Psi\rangle = A_{0,2}|0,2\rangle + A_{2,0}|2,0\rangle + A_{1,1}|1,1\rangle, \tag{3.1}$$

where the number states represent the number of photons that passes through a particular slit and $A_{i,j}$ are complex prefactors. For reasons of symmetry, the probability amplitudes $A_{0,2}$ and $A_{2,0}$ have the same amplitude and phase if the system is properly aligned. Also, in case of true far field or near field illumination, the phase difference between the three number states can be set to zero. This gives

$$|\Psi\rangle = \sin\alpha\frac{(|0,2\rangle + |2,0\rangle)}{\sqrt{2}} + \cos\alpha|1,1\rangle, \tag{3.2}$$

where α is a real-valued parameter which determines the degree at which each of the number states is present at the double slit. In Eq. (3.2), $\alpha = 0$, corresponds to fully incoherent illumination in a far-field geometry, where the position of the photons in a pair are anti-correlated due to momentum conservation. If $\alpha = \frac{\pi}{2}$, the photons always 'stick together' and pass through either of the slits in pairs. This corresponds to the situation where an image of the crystal is made on slits with a relatively large slit separation, i.e. fully incoherent illumination in a near-field geometry.

In the intermediate case of coherent illumination, where $\alpha = \frac{\pi}{4}$, the state factorizes and can be written as:

$$|\Psi\rangle = \frac{1}{2\sqrt{2}}(\hat{a}_u^\dagger + \hat{a}_l^\dagger)^2|0\rangle. \tag{3.3}$$

Where $\hat{a}_{u,l}^\dagger$ is the creation operator at the upper or lower slit, respectively. These three states serve as a simple example of complementarity: it can be seen that a state is either factorisable and coherent, or non-factorisable (i.e. entangled) and incoherent.

To determine the visibility of the two-photon interference, we write the operator for the detection of a photon as:

$$|\hat{E}_i^+\rangle \propto e^{i\phi_i/2}\hat{a}_l + e^{-i\phi_i/2}\hat{a}_u, \tag{3.4}$$

where the detectors are numbered $i = \{1,2\}$ and $\hat{a}_u, \hat{a}_l$ stand for the annihilation of a photon at the upper and lower slit, respectively. ϕ_i is the phase associated with the path length from the double slit to detector i, and $\hat{E}_i^+$ is the positive-frequency part of the electric field operator. The detection rate R_{cc} is proportional to the probability of detecting two photons:

$$
\begin{aligned}
R_{cc} &\propto \left|\langle 0|\hat{E}_1^+\hat{E}_2^+|\Psi\rangle\right|^2 && (3.5)\\
R_{cc} &\propto \left|\sin\alpha\cos\left(\frac{\phi_1+\phi_2}{2}\right)+\cos\alpha\cos\left(\frac{\phi_1-\phi_2}{2}\right)\right|^2 && (3.6)\\
R_{cc} &\propto 1+\sin^2\alpha\cos(\phi_1+\phi_2)+\cos^2\alpha\cos(\phi_1-\phi_2) && (3.7)\\
&\quad +\sin 2\alpha(\cos\phi_1+\cos\phi_2). && (3.8)
\end{aligned}
$$

To obtain the marginal one-photon visibility from this, the position of either detector must be averaged out:

$$< R_{cc} >_{\phi_2} = 1+\sin 2\alpha\cos\phi_1. \tag{3.9}$$

It is clear that this is an interference pattern with visibility $V_1 = \sin 2\alpha$.

To obtain a measure for the two-photon visibility, it is insightful to compare the extreme cases of $\alpha = 0$ and $\alpha = \frac{\pi}{2}$. In these cases, R_{cc} is a function of either $\phi_1 + \phi_2$ and or $\phi_1 - \phi_2$ alone. This suggests using the difference between the prefactors of these terms as a measure of visibility (or visibility difference):

$$V_{12} = -\sin^2\alpha + \cos^2\alpha = \cos 2\alpha. \tag{3.10}$$

In section 3.3, it will be shown that the absolute value of this measure is equal to the concurrence of the two-photon state, and that it is hence also a measure of entanglement.

Combining Eq. (3.9) and Eq. (3.10), it can be seen that

$$V_1^2 + V_{12}^2 = 1. \tag{3.11}$$

Formulated in terms of α, the parameter α traces out a semi-circle in the V_1V_{12}-plane, from $\alpha = 0$, the far-field case where there is high entanglement and high biphoton visibility, to $\alpha = \frac{\pi}{4}$ where there is no entanglement and only single-photon visibility, to $\alpha = \frac{\pi}{2}$, the near-field case where there is again high entanglement and high biphoton visibility (see Fig. 2).

3.2 Influence of defocus

If the lens that images the near field of the SPDC source onto the slits is defocused, there will be a phase difference between the pairs whose photons pass through the same slit, and those whose photons pass through different slits. In this case, Eq. (3.2) becomes:

$$|\Psi\rangle = \sin\alpha\frac{(|0,2\rangle + |2,0\rangle)}{\sqrt{2}} + e^{i\varphi}\cos\alpha|1,1\rangle, \tag{3.12}$$

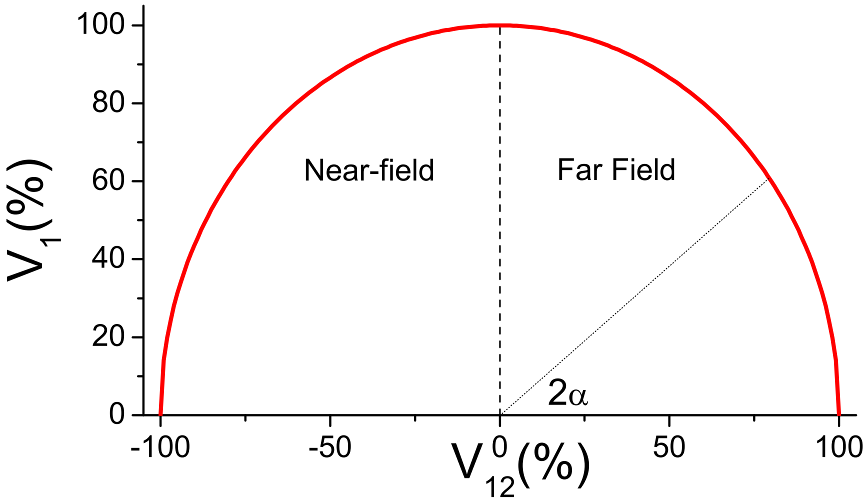

Figure 2: The complementarity curve.

where φ is the phase difference between the various possible transmission events. By repeating the calculation of section 3.1, we now find:

$$V_1 = \sin 2\alpha \cos\varphi \tag{3.13}$$

$$V_{12} = \cos 2\alpha. \tag{3.14}$$

It is seen, therefore, that those states where there is a phase difference between the different contributions to the wave function will not lie on the complementarity curve. Specifically, they will be shifted vertically toward the V_{12}-axis.

3.3 Bell states

Under the assumptions presented in paragraph 3.1, and assuming $\varphi = 0$, the Hilbert space for states at the double slit is the direct product of two identical two-level Hilbert spaces. By distinguishing the two photons via postselection, the photon field behind the double slit can be written as a linear superposition of two Bell states of the form:

$$|\Psi\rangle = \frac{1}{\sqrt{2}}[\sin\alpha(|\uparrow\uparrow\rangle + |\downarrow\downarrow\rangle) + \cos\alpha(|\uparrow\downarrow\rangle + |\downarrow\uparrow\rangle)]. \tag{3.15}$$

The Schmidt decomposition of this state is:

$$|\Psi\rangle = \frac{1}{4}\sqrt{2}(\sin\alpha+\cos\alpha)(|\uparrow\rangle+|\downarrow\rangle)\otimes(|\uparrow\rangle+|\downarrow\rangle)+\frac{1}{4}\sqrt{2}(\sin\alpha-\cos\alpha)(|\uparrow\rangle-|\downarrow\rangle)\otimes(|\uparrow\rangle-|\downarrow\rangle).$$

(3.16)

This shows the separation into the product of two symmetric and two antisymmetric terms. It also permits the calculation of the degree of entanglement or concurrence, which is defined as:

$$C = 2\left|\lambda_1 \lambda_2\right| = \sqrt{1 - \sin^2 2\alpha} = \cos 2\alpha, \tag{3.17}$$

where λ_i are the eigenvalues of the reduced density matrix of either Hilbert space. In the absence of defocus, the visibility difference $V_{12} = \cos 2\alpha$, which was put forward in eq. 3.10 is indeed a proper measure of entanglement.

3.4 Setting the coherence

The argument in paragraph 3.1 shows the complementarity between the visibility of one- and two-photon interference fringes, but it does not show the external causes of the visibilities.

For the two-photon interference pattern, the visibility is given by amount of entanglement in the two-photon field incident on the double slit. In the case of quasi-monochromatic frequency-degenerate colinear type 0 or type 1 SPCD, this field has the convenient property that it factorizes in functions of the sum and difference coordinate. It can thus be written as

$$A(\rho_1, \rho_2; z) \propto E_p(\rho_+; z)\xi(\rho_-; z), \tag{3.18}$$

where $\rho_+ = (\rho_1 + \rho_2)/2$ is the average coordinate and $\rho_- \equiv (\rho_1 - \rho_2)/2$ is half the difference coordinate. As this factorization applies to any type of imaging from the generating crystal to the double-slit, the crucial ratio

$$\tan\alpha e^{-i\varphi} = \frac{A(d,d)}{A(d,-d)} = \frac{E_p(d)\xi(0)}{E_p(0)\xi(d)}, \tag{3.19}$$

under the standard assumptions of symmetric illumination of two long narrow slits. All function should be evaluated in the slit plane.

The two-photon field is most easily evaluated in the far-field of the generating crystal. Expressed in the transverse momenta $\mathbf{q}_1$ and $\mathbf{q}_2$ of the generated photons, this field is [6]

$$\tilde{A}(\mathbf{q}_1, \mathbf{q}_2; z = 0) \propto \tilde{E}_p(\mathbf{q}_1 + \mathbf{q}_2)\tilde{\xi}(\mathbf{q}_1 - \mathbf{q}_2). \tag{3.20}$$

where $\tilde{\xi}(\mathbf{q}_1 - \mathbf{q}_2) = \text{sinc}(\frac{1}{2}\Delta k_z L)$ is the phase-matching function and Δk_z is the phase mismatch. For type 0 and type 1 SPDC, the mismatch function [7]

$$\tilde{\xi}\left(\mathbf{q}_1 - \mathbf{q}_2\right) = \text{sinc}\left(\frac{L\left(\mathbf{q}_1 - \mathbf{q}_2\right)^2}{8nk_0} + \vartheta(T)\right) \tag{3.21}$$

where n is the refractive index of the crystal with length L, $k_0 = 2\pi/\lambda_0$ with λ_0 the wavelength of the SPDC light, and where $\vartheta(T)$ is the collinear phase mismatch. The opening angle of the SPDC cone for this type of phase matching is

$$\theta_{\mathrm{SPDC}} = \sqrt{n\lambda_0/L}. \tag{3.22}$$

The description simplifies if the crystal is thin as compared to the Rayleigh range z_p of the pump laser in the crystal, making the opening angle θ_{SPDC} of the SPDC cone (much) larger than that of the pump laser. The crucial ratio defined in Eq. (3.19) thus becomes

$$\tan\alpha \approx \frac{E_p(d)}{E_p(0)} = \exp\left(-\frac{d^2}{w_{pz}^2}\right), \tag{3.23}$$

where $\varphi = 0$ and $w_{pz} = f\theta_p$ is the pump size in the slit plane, $\theta_p = \lambda_p/(\pi w_p)$ being the opening angle of a Gaussian pump with waist w_p. This ratio allows for a direct evaluation of the marginal one-photon visibility

$$V_1 = \sqrt{1 - V_{12}^2} = \frac{2\tan\alpha}{1 + \tan\alpha^2} = \frac{2\exp\left(-d^2/w_{pz}^2\right)}{1 + \exp\left(-2d^2/w_{pz}^2\right)}, \tag{3.24}$$

and the bi-photon visibility difference

$$V_{12} = \cos 2\alpha = \frac{1 - \tan\alpha^2}{1 + \tan\alpha^2} = \frac{1 - \exp\left(-2d^2/w_{pz}^2\right)}{1 + \exp\left(-2d^2/w_{pz}^2\right)}. \tag{3.25}$$

Note that $V_{12} > 0$ for the considered case of far-field illumination.

For the one-photon interference pattern, the visibility is determined by the mutual coherence between the light at the two slits. The van Cittert-Zernike theorem gives [8]:

$$V_{inc} = \exp -\frac{1}{2}(\frac{2d}{w_z})^2 \tag{3.26}$$

Where $2d$ is the slit width, and w_z is a correlation width. For a double slit which is illuminated by an $f - f$ system, $w_z = \frac{f\lambda_0}{\pi w_0}$, where w_0

From this equation, it can be seen that the three visibilities are determined by the width of the beam, and the separation of the slits.

4 Setup

4.1 General remarks

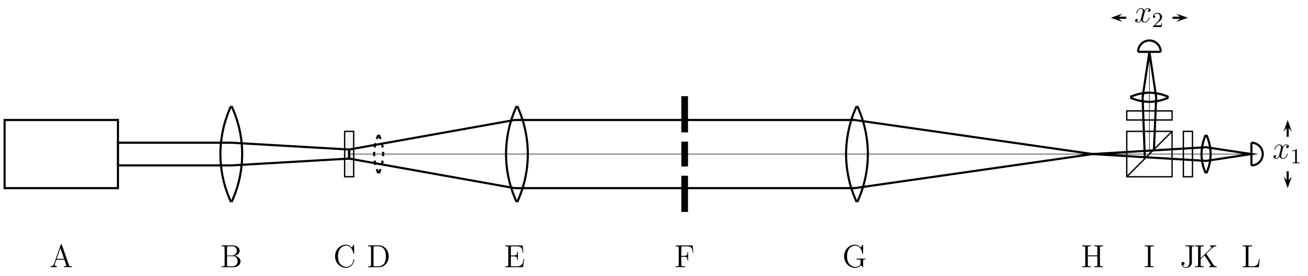

Figure 3: the experimental apparatus

The experimental setup functions as follows: 413.1 nm light from a laser at A is focused by a lens B onto a crystal of periodically poled $KTiOPO_4$ (PPKTP) at C. There, through spontaneous parametric down conversion (SPDC), photon pairs with double the wavelength of the original light are produced. After this, the pump wavelength is filtered out with a GaP-wafer (not pictured). This GaP-wafer has a transmission of 97% at the relevant wavelength.

These photon pairs are then used to illuminate the double slit at F. Illuminating the double slit can be done in two ways: either a single lens is placed at E in an f-f-configuration to produce far-field illumination onto the double slit, or with two lenses placed at D and E to image the near-field of the crystal onto the double slit.

Light which passes through the double slit is sent through another lens at G into the detection system. From the plane at H it passes through a beam splitter at I. Behind this beam splitter are two identical detectors, consisting of a narrow-band filter (J), a collimating lens (K) and a single-mode fiber (L), connnected to a single-photon detector. These fibers are movable in direction perpendicular to the optical axis, and their positions are denoted x_1 and x_2, respectively.

The counts from the single photon detectors are tallied by a counter card in the measurement computer (not pictured). Furthermore, the signals from the two single-photon counters are fed to an AND-gate to determine the coincidence count rate, and this is also tallied by the counter card.

It is convenient to name three of the planes in this setup: the plane at C is the *crystal plane*, the plane at F is the *slit plane*, and the plane at H is the *detector plane*.

The nonlinear crystal used in this experiment is the 5 mm long crystal which was procured in October 2006 from Raicol. It is kept at a temperature of 61.4 °C by a temperature control unit.

4.2 Optics

The lens at B is used to focus the laser onto the PPKTP crystal, so its focal length determines the spot waist at the crystal. Three different lenses were used; with focal lengths of 400 mm, 750 mm, and 1000 mm. These were calculated to produce spot sizes of 58 μm, 100 μm and 198 μm, respectively.

Lenses E and G are plano-convex AR-coated lenses of f=400 mm. Their position is fixed and was determined with a CCD camera so as to produce the best image of the near field of the crystal plane in the detector plane.

The collimating lenses at K are Geltech 350240 AR-coated lenses with f=8 mm and NA=0.5. They focus light onto a single-mode fiber at L, which leads to the detectors. The fiber core has a diameter of 5.6 μm at $1/e^2$ intensity. The distance between the fiber and the lenses is such that the detection mode is magnified 21 times by the microscope objective, creating a detection mode of $2w_{det}$ =118 μm in the detection plane. Stray light is filtered out by a Chroma D826/5 narrow-band filter.

In order to achieve near-field illumination, a cylinder lens is inserted at D, behind the PPKTP crystal. This lens is placed with the crystal at its focal point. This creates a two-lens system which images the crystal plane onto the double slit plane. Two lenses were used for this: one with a focal length of 40 mm, and one with a focal length of 12.9 mm, which create magnifications of 10 and 31.5 times, respectively.

The lens is mounted on a translation table, so that it can be moved both perpendicular to the optical axis and along the optical axis. The former is used for alignment, while the latter is used to achieve a defocused image of the near field of the crystal on the slit plane. The distance from the crystal to the cylinder lens is denoted z_{cyl}.

4.3 Laser

The laser used in this experiment is a Coherent Innova 300 Argon ion laser, which operates at a frequency of 413.1 nm.

There are two main issues associated with this laser. First of all, there is drift in the position and intensity of the laser spot in the period after the laser is powered up. Secondly, fluctuations in the laser power are larger than Poissonian statistics would suggest.

The first issue was analyzed by measuring the time scale of the laser drift. This was done by measuring the position of the approximate far field of the laser light over a period of 90 minutes. During this measurement, a 100cm lens was used to focus the laser beam. The measurement was done with a Spiricon LBA-FW-SCOR 20 beam profiler CCD camera, while the laser was running at full power. The results of this measurement are shown in graph 4. The intensity of the light was also monitored; this decreased by about 10% during the measurement run.

Shown in this graph is the distance which the laser spot traverses in a 90-minute time period, measured at 5 minute intervals. From this measurement a timescale for the laser drift can be extracted. It is found that the drift in laser position is well approximated by an exponential decay with the decay constant τ = 1.25 ± 0.13 h, and that the decay in laser power is well approximated by an exponential decay with τ = 0.78 ± 0.13 h. To resolve this issue, the laser was permitted to run at full power for at least 1h before measurements were commenced.

The second issue, that of fluctuating laser power, was not resolved but only characterized. By directly measuring the power, it was found that the fluctuations in power are of the order of 2%, on a time scale of 1 s. The laser has various operating modes, such as

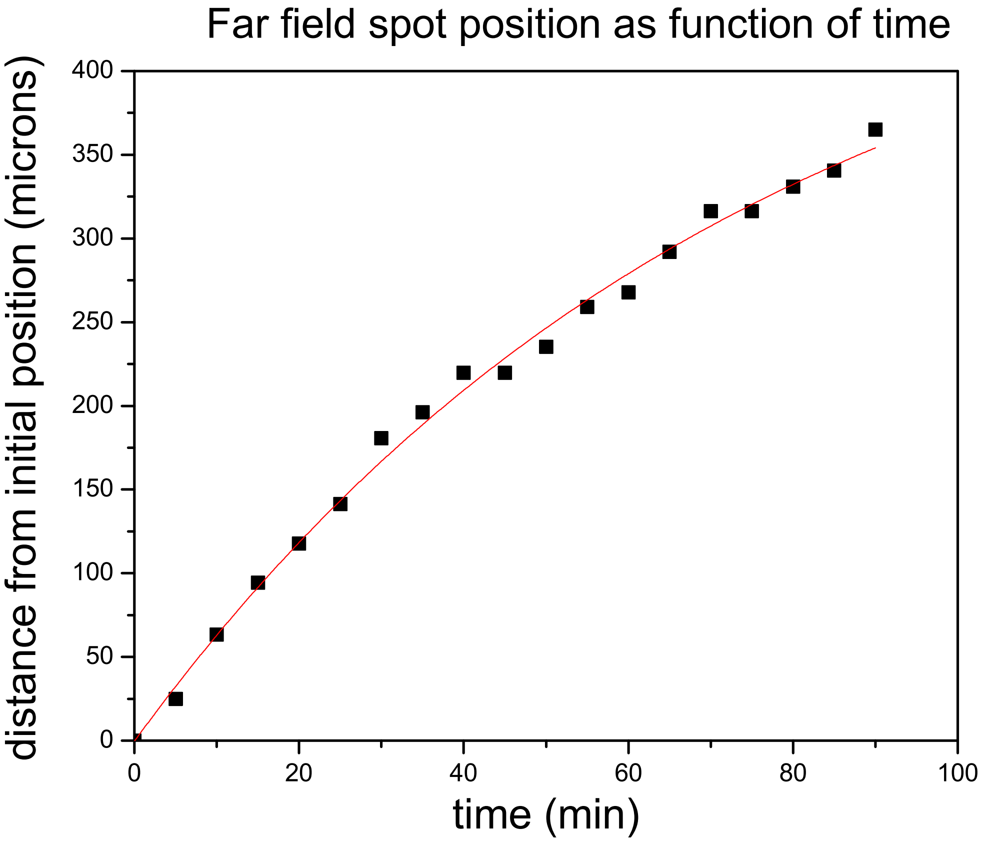

Figure 4: The drift of far field of the laser system as a function of time

’power track’ and ’light mode’, but it does not seem that these influence the magnitude of the fluctuations significantly.

4.4 Samples

For the experiment, a variety of double slit systems was required. There are two parameters in a double slit system which can be set: the heart-to-heart slit separation $2d$, and the slit width $2a$. The slit distance $2d$ influences the coherence properties of the light behind the double slit (as in a standard Young’s experiment), and hence determines the strength of the one and two-photon visibilities. The slit width $2a$ determines the width of the diffraction pattern of the individual slits, which is the limiting factor of the measurement range.

As in a regular Young’s double slit experiment, the fringes from the double slit interference can be suppressed by the zeros from the diffraction on each single slit. Since the objective of the experiment is to measure the visibility of the double slit interference, it is important that this process does not suppress too many interference fringes. The ratio d/a gives the number of fringes that are observable in the zeroth-order maximum of the far-field diffraction pattern. Given a value of d, this issue therefore places an upper limit on a. In practice, a d/a-ratio of 4 was found to be adequate for determining V_1 and V_{12}.

Besides these considerations, the slits should also be so wide as to transmit enough signal to permit a measurement within a reasonable time.

Double-slit samples were produced by two methods: electric discharge machining (EDM) and laser cutting. EDM was used to machine slits out of copper, and laser cutting was used to machine slits out of stainless steel. The slits were cut out in 25mm circular pieces of sheet metal, which are then mounted on a standard rotation mount. The slits produced by electrical discharge machining were found to be of higher quality than those made by laser etching, since the metal was less susceptible to deformation. Furthermore, the slits made by EDM were closer to specifications than those made by laser cutting.

For most slits, each design was produced several times. These copies were then examined under a microscope to select the best specimen. In one case, (slit system #4), the initial system was damaged and a replacement was selected (denoted 4b).

An overview of samples is given in table 1. In those cases where two numbers are given for the slit width, this denotes the fact that widths of two slits on one sample differ.

Table 1: Slit systems

System number	$2a(\mu\text{m})$	$2d(\mu\text{m})$	Method
1	225	1400	EDM
2	475/495	2000	Laser
3	275/255	1000	Laser
4,4b	193	600	Laser
5	137.5	312.5	EDM
6	137.5	437.5	EDM
7	380	1680	EDM
8	235	950	EDM
9	137.5	300	EDM
10	220	1400	EDM
11	135	760	EDM
12	150	515	EDM
13	75	875	Laser
14	70	850	Laser
15	80	525	Laser

4.5 Detectors

The detectors used were two SPCM-AQR-14-FC single photon counters. These are fiber-coupled to a holder which is attached to a translation stage.

The coincidence count circuit has a finite gate time, which gives rise to accidental coincidence counts (accidentals). The number of accidentals is determined by:

$$R_{acc} = \tau_{gate} R_1 R_2, \tag{4.1}$$

where τ_{gate} is the gate time. The gate time can therefore be determined by illuminating both detectors with thermal light, and recording the amount of coincidences. The results of this experiment are presented in graph 5. The gate time is found to be $\tau_{gate} = 1.73 \pm 0.01$ ns.

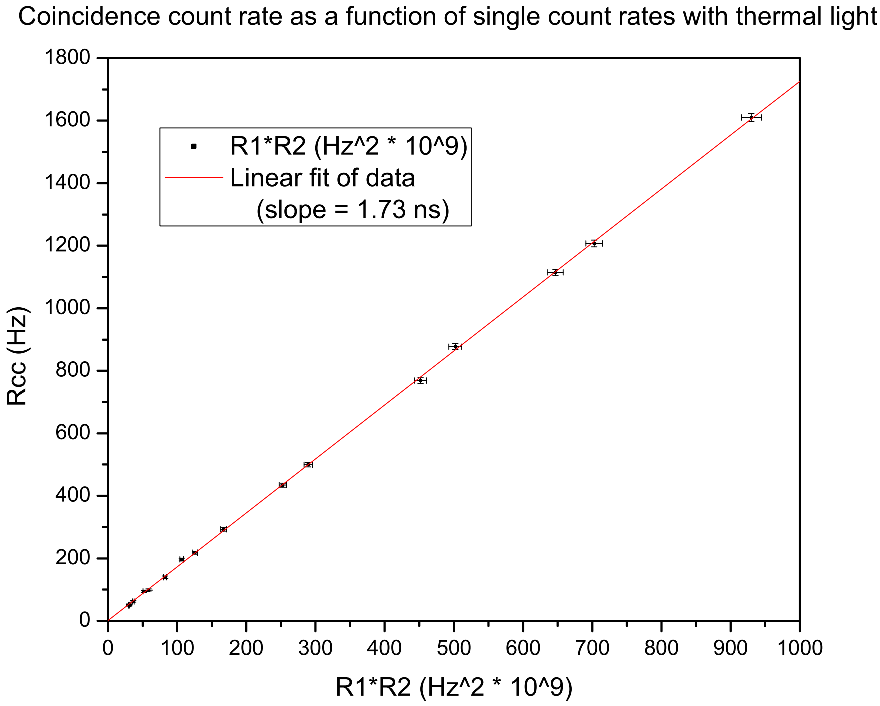

Figure 5: Coincidence count rate as function of single count rates with thermal light.

4.6 LabView system

A set of LabView VIs was built to automate the measurement process. This library consists of two components: one which positions the detectors by means of automated translation stage actuators, and the other which performs an automated scan of a series of pre-set detector positions and records the count rates at these positions.

The positioning VIs are prefixed *actuator_*. Their function is to send signals to the Newport LTA series actuators, which are used to position the detectors in this experiment. The actuators are controlled by two Newport EPS 300 motion controllers. This type of controller has a standard GPIB interface, so the LabView modules to control GPIB devices are used.

Furthermore, the motion controller has its own inbuilt programming language, based on assembler language. This language is partially supported by the LabView system: it is possible to send a series of commands in this language to the device in an initialization file. These commands are then executed before the LabView program takes control of the actuators. This is used to initialize the actuators, which is required for them to function properly. An added functionality which is not supported in the original programming is that it is now possible to add comments to these initialization files: these comments are stripped by a rudimentary parser which is built into the software.

The motion control VIs have two inbuilt protection systems to guard against improper commands being sent to the actuators. First of all, the inbuilt 'motion done' signal is used to check whether the actuators have performed the previous command before a new one is sent. Secondly, the system protects against hysteresis in the actuators by always approaching the set position from below. If the current position is above the set position, it slightly undershoots the set position and then approaches the correct position from below.

It should be noted that the accuracy with which the position of the detectors can be set is lower than the accuracy with which their position is reported by the motion controllers. The difference between the two is typically 10 nm. This difference is usually ignored by the measurement system, and the set position and the real position are assumed to be equal.

The scanning VIs are prefixed *scan_*. All VIs in this library are based on the counter card readout VI MN0102 V1.32, built by Arno van Amersfoort, which is the most recent version of this software that does not contain any known bugs. We have only modified it to make the results accessible to other LabView VIs. The other VIs in this library parse and reformat the results of the counter card VI.

Furthermore, this library also contains a series of VIs which produce, from a set of seven user-set values, an array of coordinates to be scanned. The way in which the user inputs these coordinates is separated from the rest of the program, permitting easy changes to the input system should this becomes necessary. The scan can be two-dimensional at most, and conditional positioning of either coordinate based on the value of the other is permitted.

There are two user interface VIs, *main_scan.vi* and *main_align.vi*, which are used for scanning and alignment, respectively.

A complete overview of each individual VI is given in Appendix A.

4.7 Alignment procedure

Alignment was performed in three main steps. In the first step, the positions of the detector fibers were optimized with respect to the position and angle of the pump beam. In the second step, the double slit was inserted and properly centered. In the case of near-field measurements, the last step is to insert the extra illumination lens. The details of these steps are outlined below.

In order to position the detector fibers, it is important to note the geometry of the setup. The light from the SPDC source is emitted in a cone, whose central axis is the optical axis. The intensity is spherically symmetric about this axis and has a maximum on-axis.

Each fiber has a total of five degrees of freedom: the position of the focusing lens on the optical table perpendicular to the optical axis, denoted x_{stage} and y_{stage}, and the relative position of the fiber itself to the focusing lens, denoted x_{fiber}, y_{fiber} and z_{fiber}. It is important to note that changing the stage positions shifts the focusing lens and the fiber simultaneously. Furthermore, it is important to note that the far field of the detectors (i.e. in the slit plane) is independent of x_{stage} and y_{stage}.

The x_{fiber} and y_{fiber} are positioned first, by sending light from an IR laser through them and noting the position of the detection mode in the slit plane. By using a fiber beam splitter, the two detection modes can be observed simultaneously and can be made to overlap. Then, z_{fiber} can be set by optimizing the single counts signal, though this is rarely necessary in practice. Finally, x_{stage} and y_{stage} are optimized for maximum single counts. When this is done, it is possible to check the alignment by scanning one of the two detectors. If the alignment is correct at this point, the single counts and coincidence counts will be maximal at the same x_{stage} position.

In those cases where the pump beam is narrowly focused onto the crystal, positioning by optimizing the single counts will not be very accurate. In this case, a more elaborate procedure is followed, in which the position of the fiber and of the stage of both detectors are changed simultaneously in steps which are commensurate with the magnification of the detection system. In this way, the quantum efficiency $\eta \equiv R_{cc}/R_s$ is optimized.

In step two, the slits are inserted. The only important parameter is the position of the slits in the direction perpendicular to the slits, denoted x_{slits}. The proper positioning is found by optimizing the coincidence counts as a function of x_{slits}. This positioning is then checked by measuring the coincidence counts when either of the two slits is closed off with a razor blade. Since the two detectors can have slightly different detection efficiencies, the proper criterion for proper alignment is that the ratio of the count rates of the two detectors is constant, irrespective of which slit is open.

In the case of near-field illumination, the cylinder lens is inserted in the third and last step. The focus of this cylinder lens is known from measurements with a CCD camera, so the only relevant parameter is the position perpendicular to the optical axis, denoted x_{cyl}. This position is determined by a method similar to the way the slits are positioned: first the coincidence counts are optimized, and then the balance between the left and right slit is checked closing off either of the slits with a razor blade.

5 Results

5.1 General remarks

In this chapter, the results of the measurements done on two-photon interference are shown. These measurements are of two kinds: first the introductory measurements will be shown, in which only one of the two detector positions is varied, and secondly the main, 2d-measurements will be shown, in which the positions of both detectors are varied. These will first be discussed quantitatively, and then the visibilities V_1 and V_{12} will be extracted from this latter set of measurements.

In all of the graphs that are presented in this section, R_{cc} (corrected) stands for the coincidence count rate which has been corrected for accidental counts by $R_{cc}(\text{corrected}) = R_{cc} - \tau_{gate} R_1 R_2$.

5.2 1-D Scans

In Fig. 6, the corrected coincidence count rate as a function of the position of detector 1 is shown. This measurement was done on slit system #1. For this measurement, detector 2 was placed at the center of the zeroth order of the diffraction pattern (i.e. along the optical axis). This graph was obtained by performing five consecutive scans of 0.5 s each, for a total measurement time of 2.5 s per point. As can be seen from this graph, the interference fringes predicted in Eq. (3.9) are indeed visible. Furthermore, the interference pattern is modulated by a sinc-function which is a result of the finite slit width. The measured oscillation period of 0.244 mm agrees well with the expected value $\delta x = 0.242$ mm for a slit distance $2d = 1.4$ mm in combination with $f = 40$ cm an $\lambda_0 = 826$ nm.

The error bars in this graph, and in all other graphs in this paragraph are derived by assuming that the deviations in the measured count rates are Poissonian.

In Fig. 7, the scanning detector (#1) has been moved further to the left, and the integration time has been increased to a single run of 10 s. This results in enough signal for the interference fringes present in the first maximum of the sinc to be visible. As expected, this first-order peak is half as wide as the zeroth-order peak of the sinc. This graph explicitly shows the unprecedented signal/noise ratio of our experiment.

For the last two figures, 8 and 9, the same experiment was performed, except under near-field illumination conditions. As can be seen, the results of this experiment are similar to the 1-d measurements in the far field. Integration time in both of these measurements is 10 s and it is again possible to observe the interference fringes in the first maximum of the diffraction pattern.

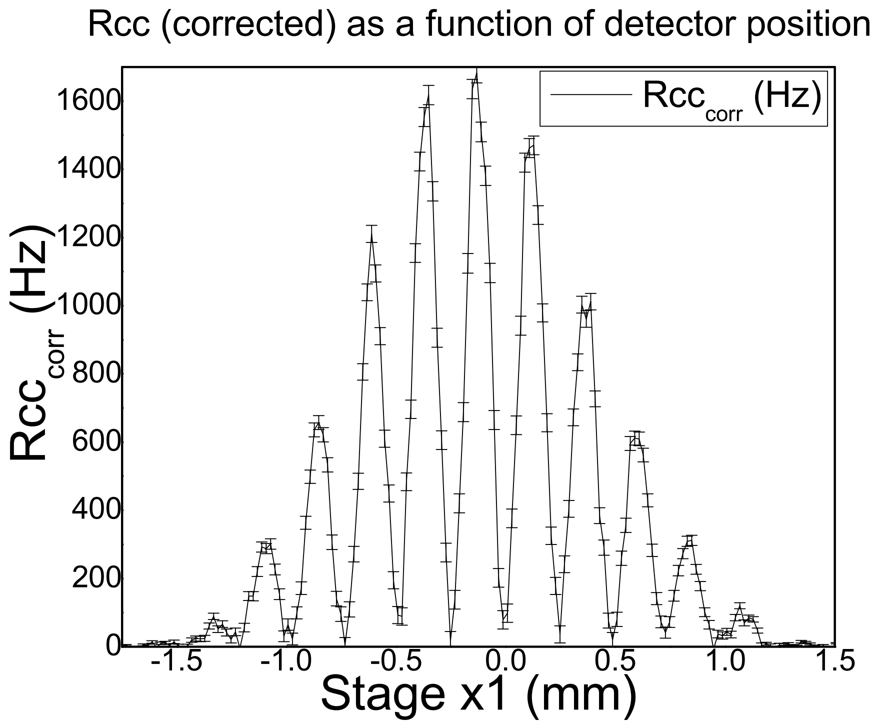

Figure 6: R_{cc} as function of detector position for far field illumination

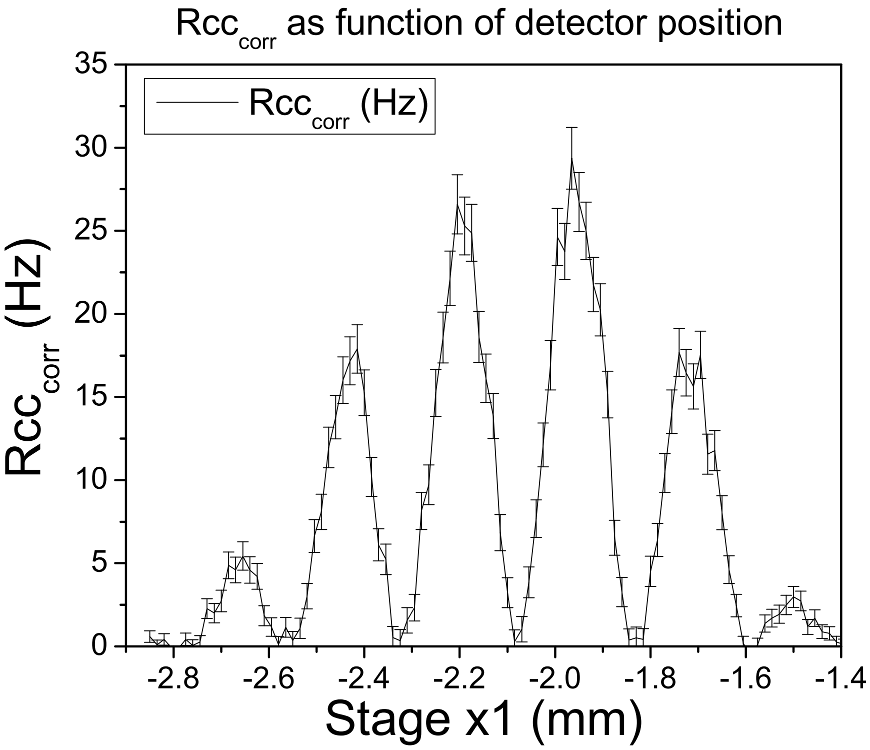

Figure 7: The interference fringes in the first-order maximum of the enveloping sinc-function for far field illumination

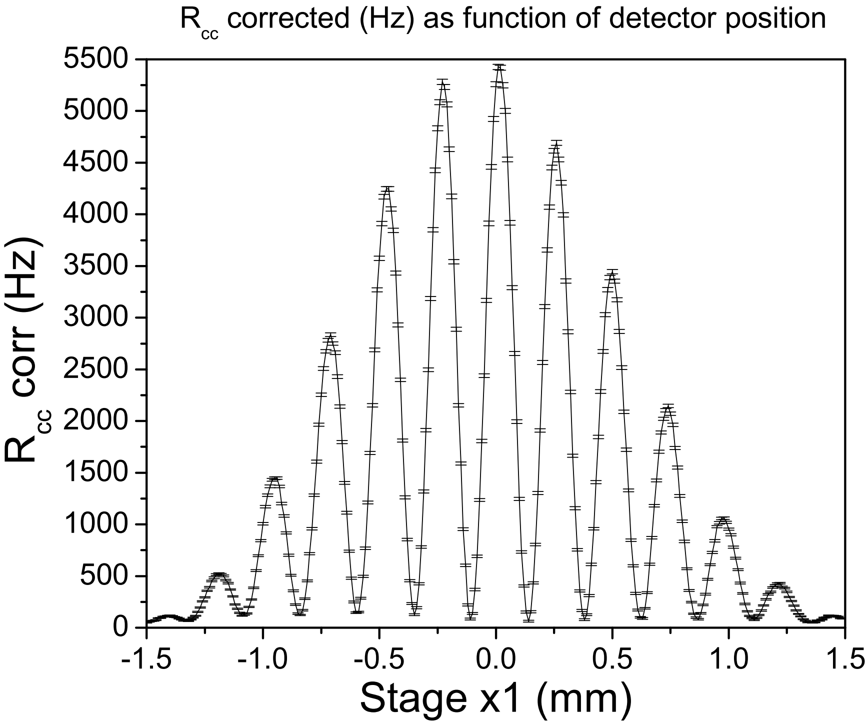

Figure 8: R_{cc} as function of detector position for near field illumination

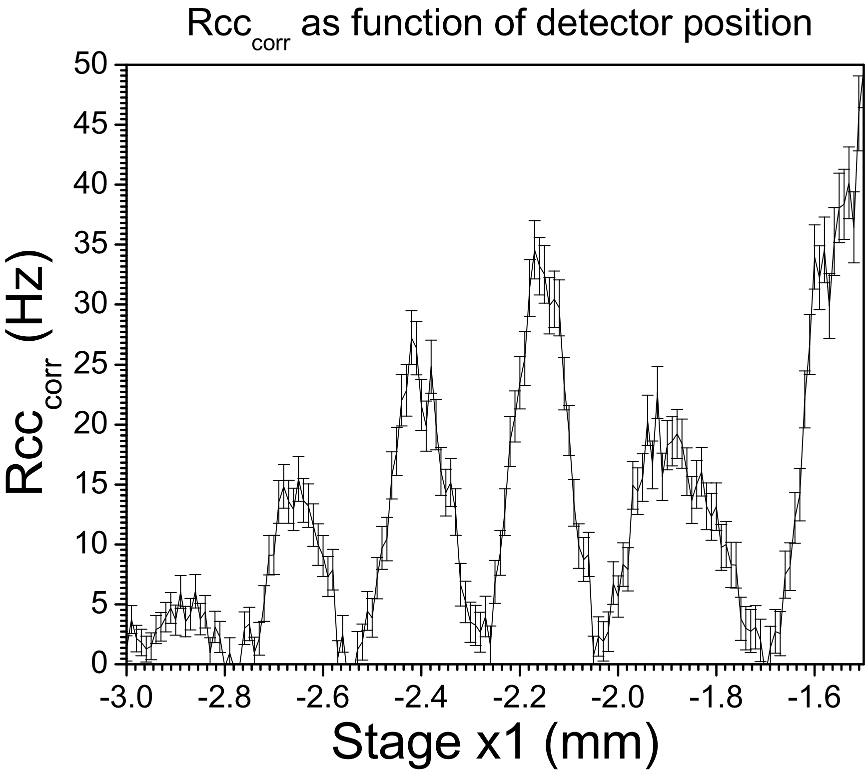

Figure 9: The interference fringes in the first-order maximum of the enveloping sinc-function for near field illumination

5.3 Typical 2d data set

In this section, the results of four 2d-measurements on slit system #1 are shown in Figs. 10 through 13. Each measurement was made by scanning detectors 1 and 2 in a grid pattern, with detector 1 performing the line scans. Integration time is 1s per point. A typical scan is a square of 1400 by 1400 μm, which is scanned with a 30 μm resolution and takes about one hour.

Entanglement is represented in these pictures by orientation of the structures which are visible in the coincidence count signal. The direction of these structures is related to the possibility to decompose the measured signal $R_{cc}(x_1, x_2)$ into a product of two functions $R_1(x_1), R_2(x_2)$ which each have only one of the two positions x_1, x_2 as a variable and are independent of the other. A periodical, grid-like structure can be decomposed in such a way, whereas for a structure which stretches along the diagonals such a decomposition is impossible, so it can be inferred that the state which was measured was entangled.

In Fig. 10, all of the structure in the measured coincidence signal is located along the diagonal axis. Therefore, the signal of detector 1 is highly dependent on the position of detector 2, which corresponds to a high degree of entanglement. In Fig. 11, the position of the 'blobs' which are visible is a separable function of detector 1 and 2, therefore there is less entanglement. The same change is visible when comparing Figs. 12 and 13.

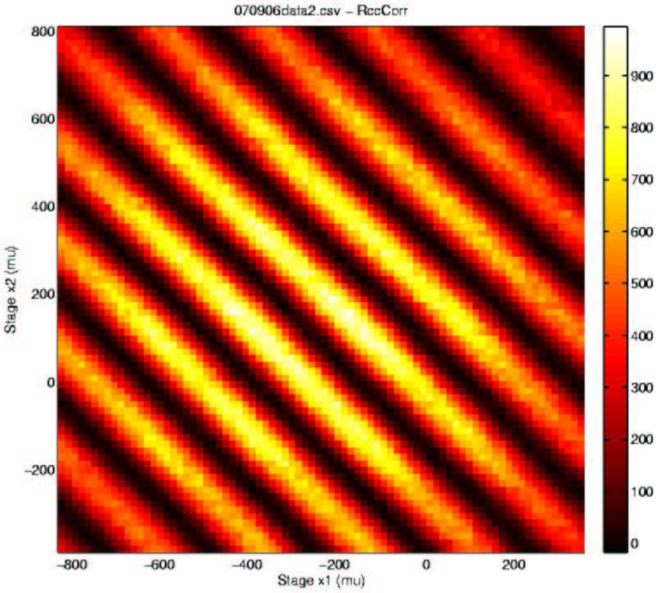

Figure 10: The two-photon interference pattern corresponding to the far field of fully entangled photon pairs

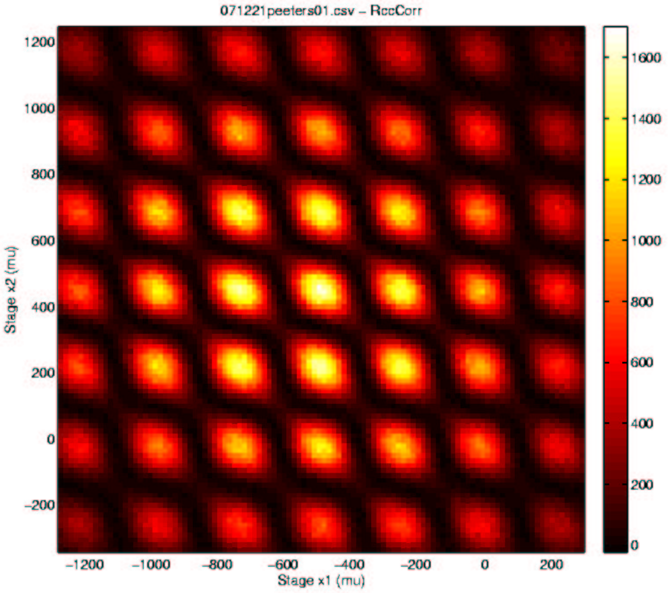

Figure 11: The two-photon interference pattern corresponding to the far field of partially entangled photon pairs

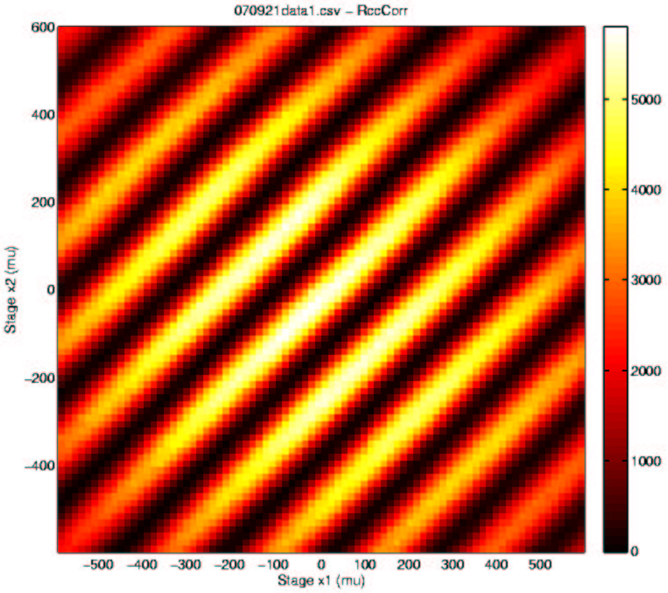

Figure 12: The two-photon interference pattern corresponding to the near field of fully entangled photon pairs

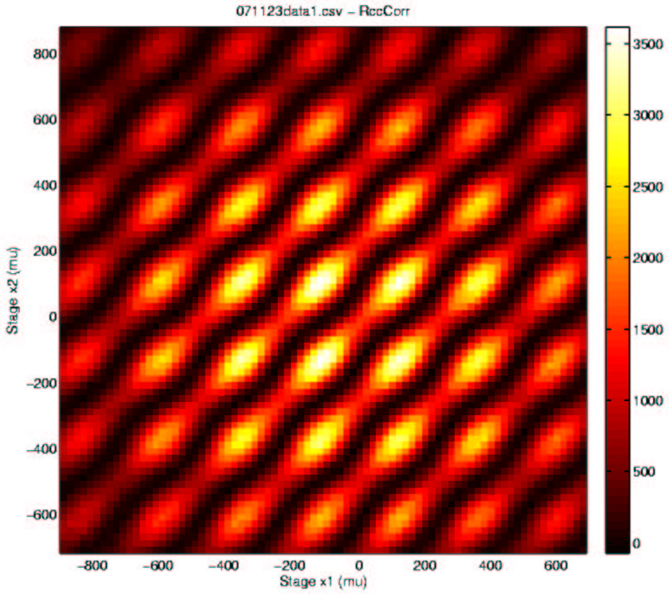

Figure 13: The two-photon interference pattern corresponding to the near field of partially entangled photon pairs

5.4 Data processing

In this section, the algorithm for extracting the visibilities V_{12} and V_1 from the graphs shown in paragraph 5.3 will be demonstrated. The data processing operations which are required for this calculation were performed by a Matlab program built for the purpose by Wouter Peeters.

Eq. (3.10) shows that the two-photon visibility difference is the difference between the prefactors of the second and third term in Eq. (3.8). Since these terms are functions of $\phi_1 + \phi_2$ or $\phi_1 - \phi_2$ only, this suggests integrating the measured coincidence signal R_{cc}, keeping the argument of either of these cosines constant. If this integration is carried out over an integer number of periods, the other terms in Eq. (3.8) disappear, and only the required term remains.

For example, to obtain $< R_{cc} >_{\phi_1+\phi_2}$ the terms in ϕ_1, ϕ_2 and $\phi_1 - \phi_2$ must be integrated out. This gives:

$$\begin{aligned} < R_{cc} >_{\phi_1+\phi_2} &\propto < 1 + \sin^2\alpha\cos(\phi_1+\phi_2) + \cos^2\alpha\cos(\phi_1-\phi_2) && (5.1)\\ &\quad + \sin 2\alpha(\cos\phi_1 + \cos\phi_2) >_{\phi_1+\phi_2} && (5.2)\\ &\propto 1 + \sin^2\alpha\cos(\phi_1+\phi_2). && (5.3) \end{aligned}$$

By similar arguments, it can be shown that

$$\begin{aligned} < R_{cc} >_{\phi_1-\phi_2} &= 1 + \cos^2\alpha\cos(\phi_1-\phi_2) && (5.4)\\ < R_{cc} >_{\phi_1} &= 1 + \sin^2\alpha\cos\phi_1 && (5.5)\\ < R_{cc} >_{\phi_2} &= 1 + \sin^2\alpha\cos\phi_2. && (5.6) \end{aligned}$$

Note that $< R_{cc} >_{\phi_1}$ and $< R_{cc} >_{\phi_2}$ provide two individual measurements of the same quantity.

The steps in this algorithm are represented in Figs. 14 through 16. In Fig. 14, the entire measurement is shown. Then, in Fig. 15, a selection of data points is made. This selection is made in such a way that the short axis of this rectangle corresponds to one period of the interference pattern. Fig. 16 is obtained by integration of the data points in the direction parallel to the short axis. The data points then are automatically fitted to Eq. (5.3, multiplied by an appropriate envelope function. This fitting is done by the least-squares method; the initial parameters for this process are determined by heuristic methods.

Note that both the V_1 and V_{12} are reconstructed from the measured coincidence count rate. It is also possible to extract a third visibility of the interference pattern, V_{inc}, from the uncorrelated (single) counts of each of the detectors. This is demonstrated in figures 17 and 18, where the single count rate from detector 1 is shown. This data was taken from the same measurement from which Fig. 14 was extracted. Note that in general, $V_{inc} \neq V_1$. The reason for this is that the single count signal is dominated by those events where the second photon does not pass through the double slit.

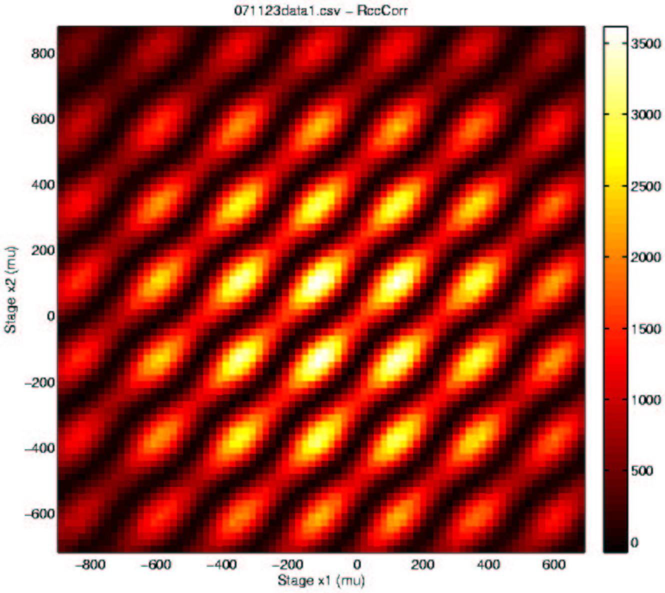

Figure 14: A typical measurement

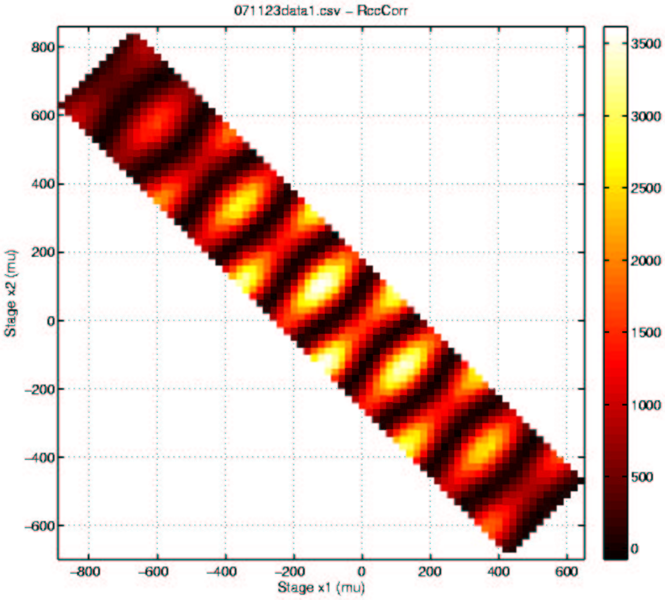

Figure 15: The measurement cut along the diagonal axis

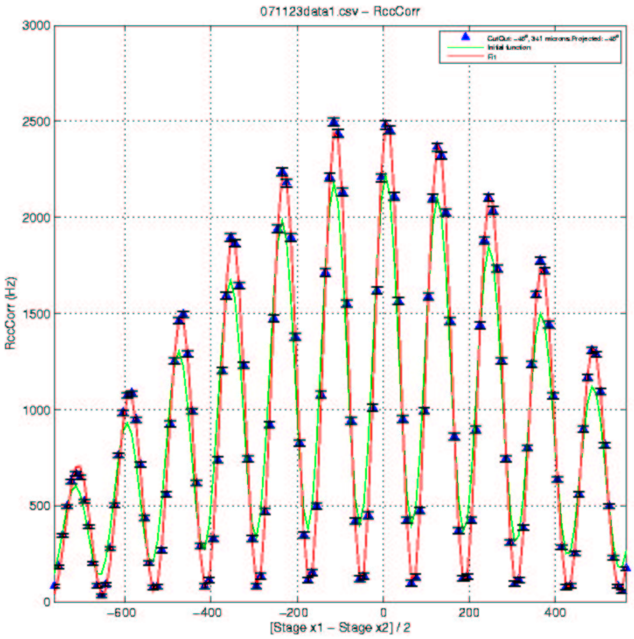

Figure 16: Interference fringes along the diagonal axis

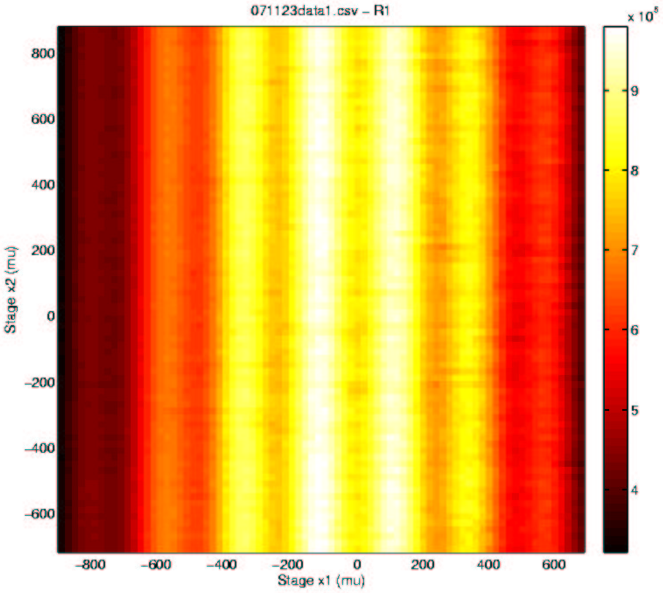

Figure 17: the single count signal from the same measurement

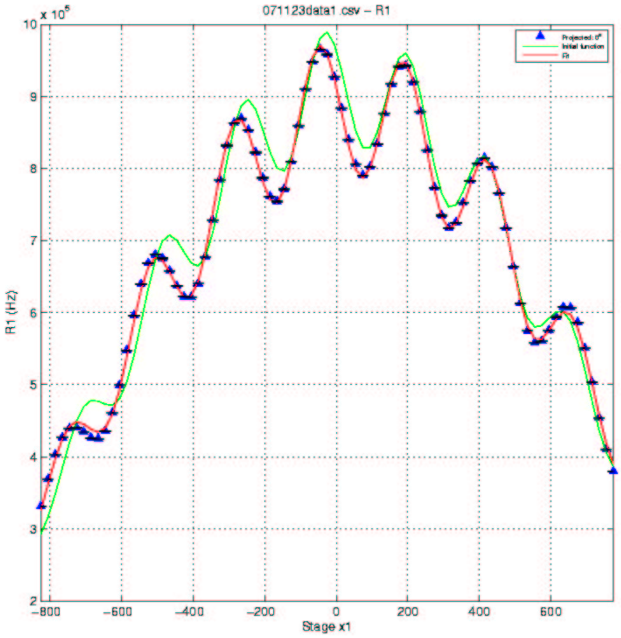

Figure 18: Oscillations in the average single counts, obtained through projection of Fig. 17 onto its horizontal axis

5.5 Complementarity curve

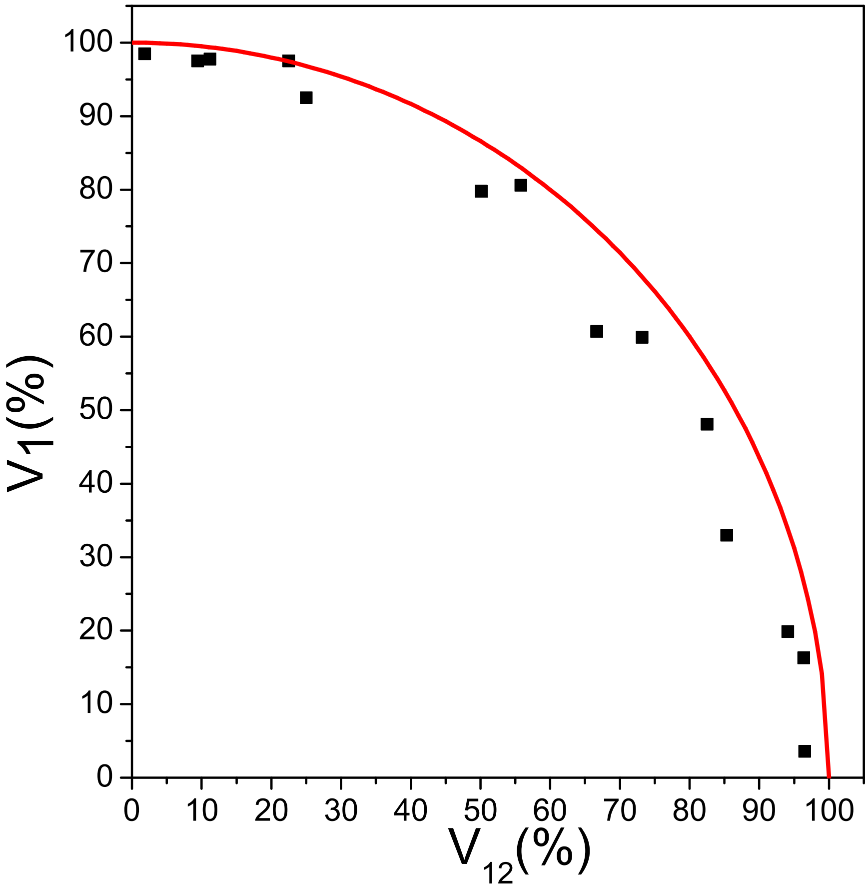

Figure 19: Complementarity in the far field

Measurements similar to the ones reported in section 5.3 were performed under various illumination conditions, and with various double slit samples. The marginal one-photon visibility V_1 and the two-photon visibility difference V_{12} were then extracted by means of the algorithm described in section 5.4. In this way, the complementarity curve (Fig. 2) was probed. The results of this are presented in Figs. 19 and 20.

In Fig. 19, the measurements in the far field are shown. In this graph, it can be seen that it is possible to probe the complementarity curve from the case $(V_1 = 0, V_{12} = 1)$, where there is maximal entanglement and no coherence, to the case where $(V_1 = 1, V_{12} = 0)$, where there is no entanglement and full coherence. The case of the near field is shown in Fig. 20. The results in the near field can be interpreted similarly as the ones in the far field.

The error in determining the visibilities V_1 and V_{12} from the measured data is less than 1%, assuming that the errors on the measured count rates are Poissonian in nature. In

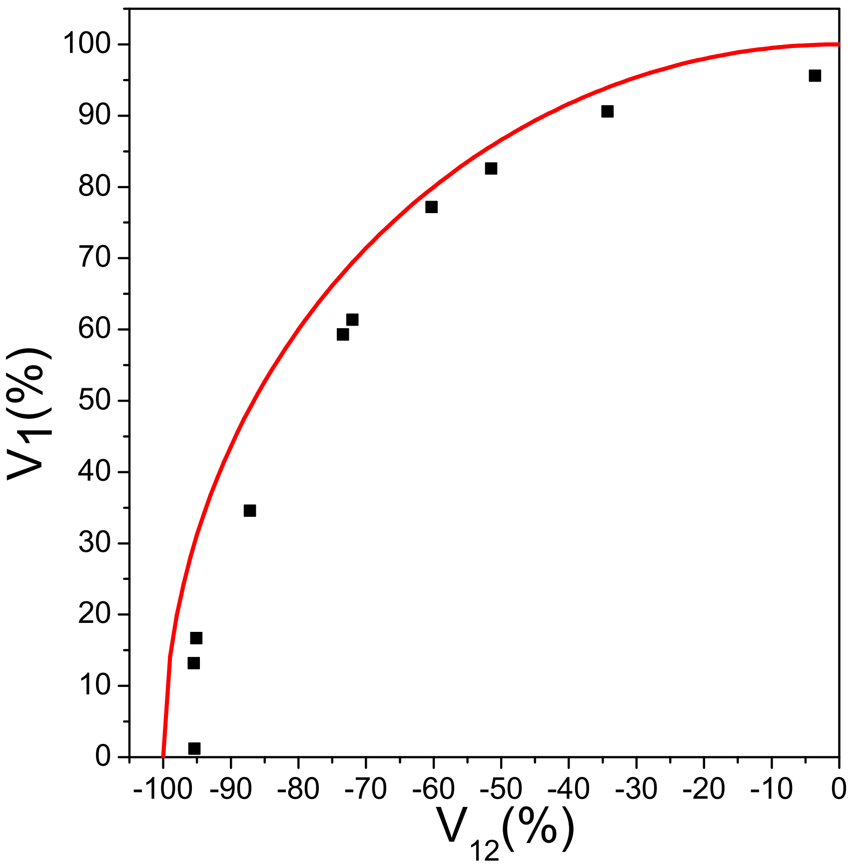

Figure 20: Complementarity in the near field

a few instances, the experiment was repeated under identical conditions. The spread in results which were obtained from these identical runs suggest an error of about 2%. Further deviation between the measured points and the theoretical curve is thought to be due to alignment problems. Simulations show that errors in alignment always reduce the visibility of the interference fringes.

5.6 Measurements as function of slit separation

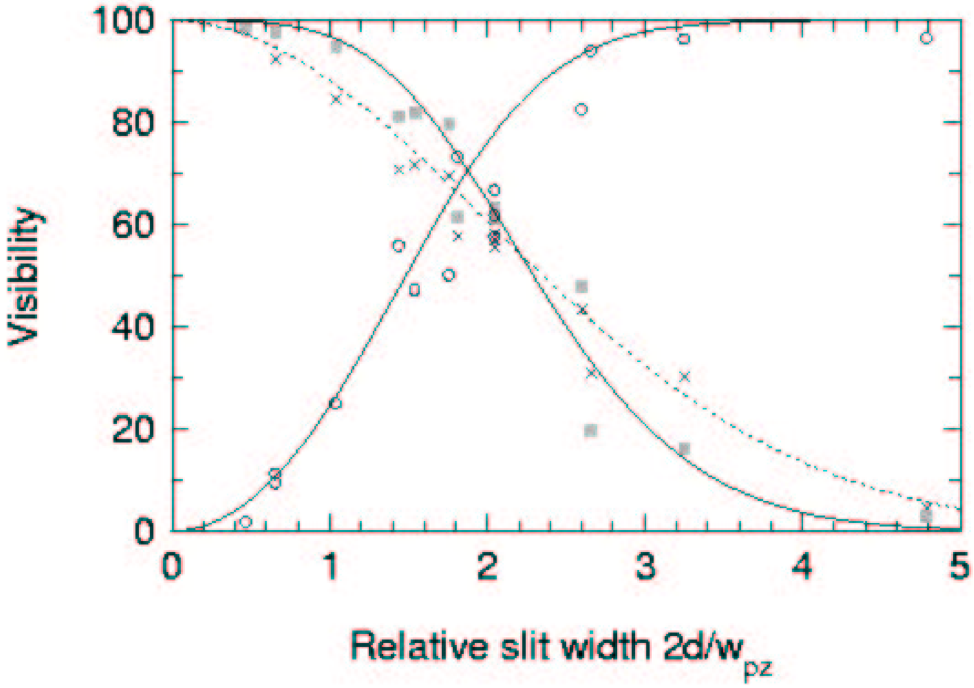

Figure 21: V_1, V_{12} and V_0 as a function of slit separation, under far field illumination

In this section, an alternative method of visualizing the results of the two-photon experiments is presented. Whereas the results of the two-photon experiments are normally presented in the context of complementarity, it is also possible to ignore this notion and show both the one and two-photon visibilities as a function of the slit width. Under far-field illumination, it is most relevant to present these results in terms of the relative slit width $2d/w_{pz}$, which is the slit width normalized by the SPDC spot size. Under near-field illumination, the relevant parameter is $2d/M$, where M is the magnification. These results are shown here without further comment.

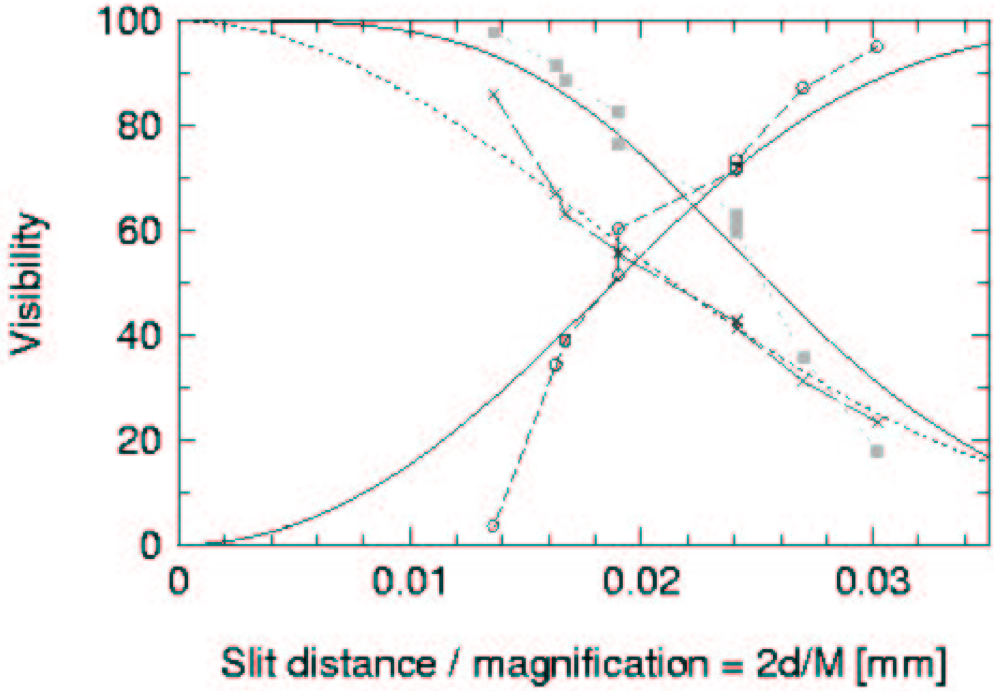

Figure 22: V_1, V_{12} and V_0 as a function of slit separation divided by magnification, under near field illumination

5.7 Defocus points

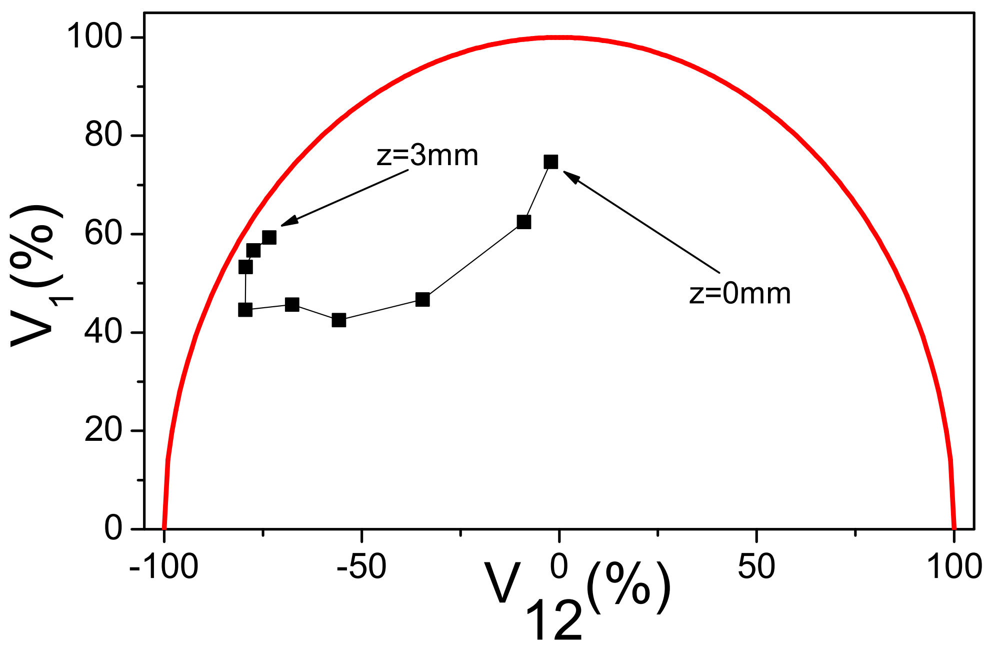

Figure 23: V_1 and V_{12} as a function of z_{cyl}

The measurements done under near-field illumination suggest another way to change the parameters α and φ in Eq. (3.2), namely by defocusing the imaging lens. However, defocusing the imaging lens will result in a nonzero φ, which leads to reduction of the two-photon visibility.

In order to test this, a series of two-photon interference experiments were done on slit system #11. The cylinder imaging lens was moved from $z_{cyl} = 3$ mm to $z_{cyl} = 1$ mm, in steps of 0.25 mm. The results of this experiment are shown in Fig. 23.

The variations in V_1 and V_{12} are intriguing and as yet not well understood. Repeating the experiment for some values of z_{cyl} has shown the experiment to be reproducible. Furthermore, defocussing by increasing instead of decreasing z_{cyl} (i.e. $z_{cyl} > 3$mm) has produced similar results. Also of note is that the unconditional visibility is almost unaffected by the defocussing, changing from $V_{inc} = 0.42$ at $z_{cyl} = 3$mm to $V_{inc} = 0.46$ at $z_{cyl} = 1$mm. None of this behavior is as yet theoretically understood.

5.8 Determination of A_{ll}, A_{lr}, A_{rl}, A_{rr}

by near-field detection.

In order to probe the exact illumination of the double slit under experimental conditions, we used an optical system for near-field detection was performed. In this system, an $f = 300$mm lens was placed between the second lens (lens G in figure 3) and the detection plane. This lens serves to image the slit plane onto the detector plane. This makes it possible to tune each detector to only receive signal from a single slit. In this way, it is possible to determine individually the amplitudes A from eq. 3.1.

Near-field detection was sometimes also used as an alignment trick when centering the double slit and the SPDC light. It should be noted that in this setup, the independence between aligning the near field and aligning the far field which was noticed in section 4.7 is no longer present. This is due to the fact that the imaging system is not a perfect $f - f$ system.

However, under near-field illumination, the near field of the crystal is imaged onto the slit plane by a system of two lenses. Since the slit plane is in turn imaged onto the detection plane, this means that the detectors are in the near field of the SPDC crystal. This suggests using this setup to investigate the properties of the SPDC crystal.

A small experiment into this direction was performed, of which the results are shown in this paragraph. By translating the first lens of the imaging system along the optical axis, it is possible to perform a scan of the SPDC crystal. The results of this experiment are shown in figure 24. The subscripts l and r refer to the left and right slit, e.g. A_{lr} is the coincidence count rate when detector one is aimed at the left slit and detector two at the right slit. Through measurements with a CCD camera, it was determined that the cylinder lens has the best focus when $z_{cyl} = 3$.

An interesting fact to note is that it is clear that the 'bunched' count rates (those where the photons pass through the same slit) have two clear cutoff points, at $z = 1.8$ and $z = 4.6$. Theoretically, we expect the separation between these points to be equal to the crystal thickness, divided by the refractive index $n = 1.83$. Since the thickness of the crystal $L = 5.07mm$, the obtained ratio $L/n = 2.78$ is in good agreement with our measurement.

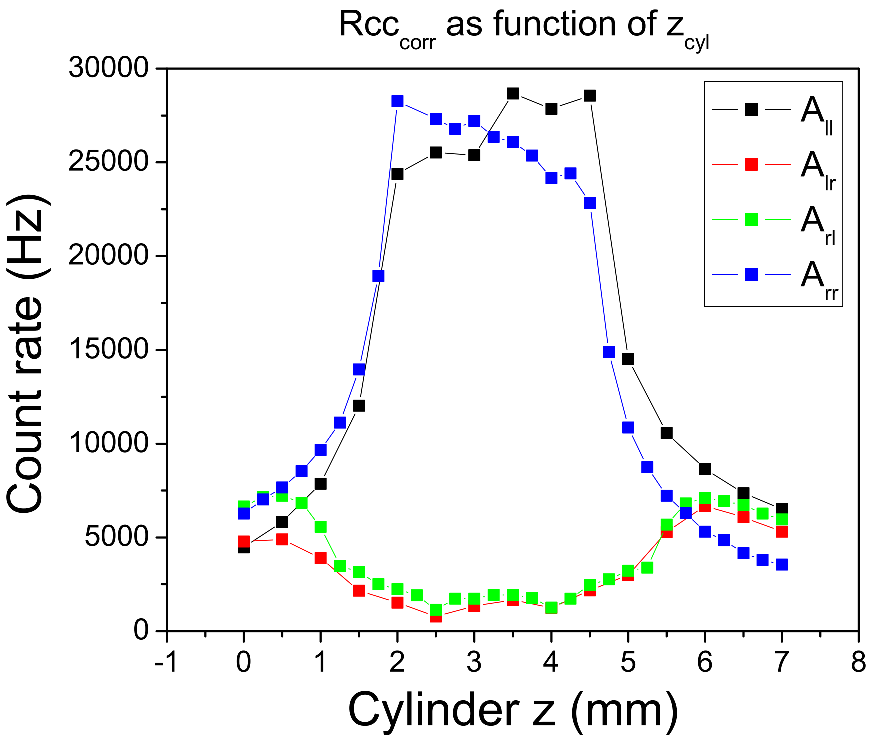

Figure 24: The coincidence signal per slit combination as a function of z_{cyl}

6 Summary, conclusions and outlook

In this experiment, various forms of interference of photon pairs at a double slit have been investigated. This has been done by illuminating multiple double slit samples with light from an SPDC source and recording the coincidence counts at two single-photon detectors located behind the sample.

This measurement has been done under two illumination conditions, namely for illumination of the sample in the far field of the SPDC crystal and for near-field illumination. In both of these cases the important feature of *complementarity* between the visibility V_1 of the interference fringes of the conditional single photon count rates and the visibility difference V_{12} of the coincidence count rate has been experimentally demonstrated. We have also introduced a third visibility V_{inc} for the unconditional (or incoherent) singe photon count rate, which has so far played only a marginal role in the analysis, but could be of interest for future research.

These measurements present a significant expansion of earlier work [4] [5] in several ways. Most importantly, we have probed new areas of the parameter space, specificaly the area of near-field and defocused illumination. The measurements show an unprecedentedly high signal-to-noise ratio. This is due to the use of a brighter periodically poled KTP source of photon pairs, as well as the use of a less wasteful design of the optics which collect the light from the double slit to the detectors. Furthermore, we have introduced a new analysis procedure which permits easy interpretation of the state which is present at the double slit in terms of the mixing of two Bell states, with a mixing angle α. We have also introduced an algorithm for data reduction which enables us to retrieve the one-photon and two-photon visibilities to a high degree of accuracy.

Pursuing the main line of research, two topics have arisen: first of all, it seems possible to use the double slit as a probe to investigate correlations between the two-photon field at different positions, and thereby study the near-field structure of the light emitted by the SPDC source. Secondly, defocussing the illumination of photon pairs onto a double slit under near-field gives results which have so far not been adequately explained. It is likely that these two phenomena will be subject to further research, either in the context of a deeper investigation of two-photon interference, or in the context of quantum state engineering.

A LabView routines

A.1 Main_scan.vi

The main VI used for making scans.

Inputs

- none

Outputs

- none

Known issues

- none

A.2 Main_align.vi

The main program used for alignment. This program can be used to position the actuators and to get readings from the counter card.

Inputs

- none

Outputs

- none

Known issues

- The Y-scale of the graphs scales as the maximum of all measured values, not as the maximum of the values which are on the graph.
- The connection between the actuators and the GPIB addresses is hardwired, and needs to be changed for the next experiment.

A.3 Actuator_bundle.vi

This program combines the various pieces of data about an actuator into a single datastructure, which is then used by all other programs to retrieve information about the actuator.

Inputs

- Adress string (string) : the GPIB address of the actuator
- Initialization data (array of strings) : a series of commands which is sent to the actuator when it is initialized
- Error in (cluster): the standard LV error structure
- LVBacklash (double, millimeters): the size of the backlash loop as implemented in LV.
- Axis name (string): The name of the axis which the actuator is on. This is not used by any program but is for identification
- Axis number (double): the axis number. A number identifying which port on the EPS controller the actuator is connected to. This is used in conjunction with the address string for sending commands to the actuator.

Output

- Actuator bundle (cluster)

A.4 Actuator_getposition.vi

Reports the position of the actuator in millimeters. This is with respect to the (arbitrary) zero given by the EPS controller.

Inputs

- Actuator handle (cluster)

Outputs

- Actuator handle (cluster)
- Position (string, millimeters) the position as a double encoded in a string

Known issues

- The string needs to be converted into a double by use of the proper operator. The standard string-to-number operator converts strings to integers.

A.5 Actuator_init.vi

Takes the input required to assemble an actuator handle and assembles the handle. Then, it sends the required commands to the actuator to initialize it.

Inputs

- The same as actuator_bundle.vi

Outputs

- Actuator_handle (cluster)

A.6 Actuator_initfileparse.vi

This program parses the init files, for which we use a custom-built system which allows for comments. These comments are stripped, and the file is converted into an array of strings.

Inputs

- File (address) the address of the init file
- Error in (cluster) the standard LV error handle

Outputs

- Initialization data (array of strings): an array of strings to be sent to the actuator.
- Error out (cluster): the standard LV error handle

A.7 Actuator_sendinit.vi

Sends a series of commands, as specified by the actuator init file, to the actuator.

Input

- Actuator handle (cluster)

Output

- Actuator handle (cluster)

A.8 Actuator_setposition.vi

Sets the position of the actuator to a position specified by Set Position. It also checks whether the current position is higher than the set one, and implements a backlash correction routine if this is the case.

Input

- Actuator handle (cluster)
- Set Position (double, millimeters): the position which the actuator is to be set to.

Output

- Actuator handle (cluster)
- Motion done (Boolean): a Boolean which is false, which becomes true when the motion is done. This is redundant is the next VI to be executed accepts an actuator handle.

A.9 Actuator_setpositionCORE.vi

The core VI which sets the position of the actuator. Flow control (waiting for the motion to be done before allowing the flow to continue) is also done in this VI.

Inputs

- Same as actuator_setposition.vi

Outputs

- Same as actuator_setposition.vi

A.10 Actuator_unbundle.vi

Performs the inverse operation of actuator_bundle: it separates the actuator handle into the separate pieces of data which are contained in it.

Inputs

- Actuator handle (cluster)

Outputs

- Adress string (string) : the GPIB address of the actuator
- Initialization data (array of strings) : a series of commands which is sent to the actuator when it is initialized
- Error in (cluster): the standard LV error structure
- LVBacklash (double, millimeters): the size of the backlash loop as implemented in LV.

- Axis name (string): The name of the axis which the actuator is on. This is not used by any program but is for identification
- Axis number (double): the axis number. A number identifying which port on the EPS controller the actuator is connected to. This is used in conjunction with the address string for sending commands to the actuator.

A.11 Scan_appendgraph.vi

The program appends one data point to an array of points, which is in a suitable data format to be plotted on a chart or graph. It should be used in conjunction with a shift register to continuously update some graph, or to build an array which is to be written to a file. It can also generate an empty array.

Inputs

- Boolean (Boolean): If this is set to True, the VI takes the array from Array and appends a point to it. If not, it generates an empty array.
- Array (2d array of doubles): the array of previous points
- X (double): the x-coordinate of the point which is to be appended to this array
- Y (double): the y-coordinate of the point which is to be appended to this array.

Outputs

- Output array (2d array of doubles): the appended array.

A.12 Scan_convertarray.vi

Converts the initialization values for the array of scan-positions to a form accepted by scan_generate_array.vi. Note that this program takes its inputs in microns and returns values in millimeters.

Inputs

An input cluster with inputs from the user interface of scan_main.vi. This consists of:

- Offset per outer loop position: the amount by which the entire inner scan needs to be displaced per unit of length when the outer scan is moved. A dimensionless quantity
- Inner step size: the step size of the inner loop (in microns)
- Inner half width: the half width of the inner loop (in microns)

- Inner center: the center point of the inner loop scan in the case that the outer loop is at its center (in microns)
- Step size: the step size of the outer loop (in microns)
- Half width: the half width of the outer loop (in microns)
- Center: the center point of the outer loop (in microns)

Note that the program is constructed in such a way that the step size can be overridden by the half width and center settings: the step size is always chosen in such a way that center-HW, center and center+HW are included as points.

Outputs

Output cluster: an output cluster which is accepted by scan_generate_array.vi. This consists of:

- Start0 : the starting position of the inner loop on the first scan run, in millimeters
- N1: the number of points to be scanned in the outer loop
- N0: the number of points to be scanned, per run of the outer loop, in the inner loop
- L0: the step size of the inner loop, in millimeters L1: the step size of the outer loop, in millimeters
- Start1: the starting position of the outer loop on the first scan run, in millimeters
- Delta: the amount by which the inner loop has to be displaced after each run, in millimeters.

A.13 Scan_create_empty_array.vi

Creates an empty measurement data cluster. This cluster consists of three 2d arrays of doubles which contain the X-Y values which are printed on the graphs on screen, and a 2d array of doubles which contains the data which is written to files

Input

- none

Output

- Cluster (cluster) a data cluster as described above

A.14 Scan_generaterarray.vi

Generates an array, which contains the coordinates of the points to be scanned. This VI takes an input cluster containing the information about the array which is to be generated, as specified in the description of scan_convertarray.vi.

Inputs

- Input cluster (cluster): see scan_convertarray, where it is an output cluster.
- Outer loop active (Boolean): if set to true, the settings for the outer loop are not considered when generating the array. They are undetermined.

Outputs

- Array (2d array of doubles, millimeters): an array of points, with outer and inner loop position for each point to be scanned.

A.15 Scan_getcoords.vi

A small VI which separates a single point from the coordinate array (which comes out of scan_generatearray.vi) into the inner and outer loop position, both in microns.

A.16 Scan_saveandappend.vi

Appends the data from a single point to the measurement data cluster.

Inputs

- 1 point-data (1d array of doubles): an array consisting of:
    - inner position (in millimeters)
    - outer position (in millimeters)
    - R1 (kHz)
    - R2 (kHz)
    - Rcc (Hz)
- Coinc*0.01? (Boolean) A Boolean which determines whether the coincidence count is multiplied by 0.01. note that this is done for display purposes only, the true coincidence count is always recorded in the section of the measurement data cluster which is written to a file.
- Input data cluster (cluster): the measurement data cluster which is to be appended

Outputs

- Output data cluster (cluster): the data cluster with the new point appended to it.
- To graph (cluster): The data cluster converted into an array of clusters, each containing a single array of sets of x-y values. This is the form which is suitable for plotting in LV graphs.

A.17 Scan_savedata.vi

Saves data to a file.

Input

- Cluster (cluster): A measurement data cluster. This cluster is stripped and the part which is to be written to a file is written to the file specified in the dialog path.
- Save Data (bool): the boolean which triggers saving the data.

Output

- Cluster2 (cluster): The measurement data cluster. Currently this connector is not used; it can be useful as a flow control tool.

A.18 Scan_scanwrapper.vi

A wrapper around the coincidence counter VI. This VI uses coincidence counter V1.32 (the last version made by Arno, later versions are by Erwin and others).

This VI also collects the position data and the coincidence rate into a single array.

Input

- Inner loop pos (double, millimeters): the position of the inner loop
- Outer loop pos (double, millimeters): the position of the outer loop
- Scan time (double, seconds) : the scan time

Output

- One point data (1d array of doubles). For specification, see scan_saveandappend.vi, where this array is an input.

A.19 Scan_time.vi

A VI which estimates the time it takes to complete a scanning run. Currently, this is a very rough estimate, and it is generally accurate to within a factor of 2.

Inputs

- input cluster (cluster): the input cluster which goes into scan_generate_array.vi
- scan time (double, seconds): the scan time per point in seconds

Outputs

- total scan time (double, minutes): the total scan time, in minutes

B Overview of measurements

B.1 Introduction

In this appendix, a complete overview is given of all measurements done in the period from July 2007 to December 2007. This is done in two tabels, one for far-field measurements and one for near-field measurements, including defocussed measurements.

A full overview of all tabulated values follows:

- *File name* is the name of the file in which the data is originaly saved. All files carry the .csv extension.
- M is the magnification of the near-field imaging lens.
- z_{cyl} is the position of the near field imaging lens, measured in mm from the crystal.
- *pump* is the size of the pump beam on the crystal, in microns.
- *slit* is the slit number
- V_{45} is the visibility along the 45 degree axis
- V_{-45} is the visibility along the -45 degree axis
- V_{12} is the biphoton visibility (i.e. $V_{-45} - V_{45}$)
- V_0 is the conditional visibility along the x-axis
- V_{90} is the conditional visibility along the y-axis
- $V_{0,inc}$ is the unconditional visibility along the x-axis
- $V_{90,inc}$ is the unconditional visibility along the y-axis

B.2 Table of measurements

Table 2: Far-field measurements

File name	pump	slit	V_{45}	V_{-45}	V_{12}	V_0	V_{90}	$V_{0,inc}$	$V_{90,inc}$
070727data3	180	1	89.7	0.8	88.9	26.4	33.4	6.3	7.1
070906data2	180	1	96.6	0.1	96.5	3.6	2.4	4.7	4.5
071002data1	58	1	66.8	19.6	47.2	82.4	81.57	71.9	71.4
071005data4	58	5	52.8	51	1.8	98.5	99.3	98.5	97.7
071023data1	58	8	61.9	36.88	25.02	92.5	97	84.8	84.6
071026data1	58	4	52.3	42.9	9.4	97.5	97.7	92.7	91.9
071029data1	58	4	54.7	43.5	11.2	97.8	97.7	92.7	92
071128data1	180	11	90.9	8.4	82.5	48.1	47.9	43.7	43.3
071128data2	180	8	97.8	1.43	96.37	16.3	16.3	29.9	30.4
071130data1	180	5	63	40.5	22.5	97.5	97.5	88.2	87.8
071203data1	180	12	74	23.9	50.1	79.8	79.6	69.7	69.5
071204data1	180	4	74.3	16.7	57.6	65.1	61.5	58	58
071205data1	180	4	82.4	15.73	66.67	60.7	61.29	56.9	57.1
071205data2	180	–	79.8	18	61.8	63	63	56	55
071205data2	180	4b	79.8	18	61.8	63	63	56	55
071206data1	100	1	65.8	10	55.8	65	64	30	30
071207data1	100	1	60.1	2.6	57.5	65.9	69.7	30	30
071207data4	100	1	90.6	5.3	85.3	33	32.7	30	30
071209data2	100	1	94.8	0.7	94.1	19.9	19.7	30.8	30.8
071209data3	100	8	84.9	11.7	73.2	59.9	62.8	57.8	57.8
071209data4	100	11	78.2	22.4	55.8	80.6	81.7	70.5	70.8

Table 3: Near-field measurements

File name	M	z_{cyl}	pump	slit	V_{45}	V_{-45}	V_{12}	V_0	V_{90}	$V_{0,inc}$	$V_{90,inc}$
070920data12	10	-	180	1	0.1	81.9	-81.8	18.5	26.6	0.2	0.5
070921data1	10	-	180	1	0.4	95.8	-95.4	1.2	1.2	0.2	0.1
070924data2	10	-	180	1	0.3	81.5	-81.2	18.6	20.8	0.2	0.3
071011data2	31.5	-	58	1	3.4	86.5	-83.1	19.8	20.7	6.8	6.5
071018data1	31.5	3	58	1	5.2	88.1	-82.9	37.8	39.7	7.8	7.7
071018data2	31.5	2	58	1	5.1	89.4	-84.3	20.7	22.1	6.4	6.2
071018data3	31.5	1	58	1	26.8	64.6	-37.8	37.7	39.8	4.7	3.2
071019data1	31.5	0.5	58	1	40.7	51	-10.3	9.91	16.35	6	5.3
071019data2	31.5	0	58	1	46.5	46.3	0.2	28	30	8.6	7.8
071019data3	31.5	2.5	58	1	3.2	91.3	-88.1	14.1	16.2	7.3	6.8
071022data1	31.5	3	58	5	48.9	52.5	-3.6	95.6	100	86	85.8
071022data2	31.5	0	58	5	50.4	50.1	0.3	96	99	86.6	85.8
071023data2	31.5	3	58	8	1.9	97	-95.1	16.7	19.2	23.4	23.6
071025data1	31.5	3	58	11	12	84	-72	61.4	63.4	43.2	42.9
071025data2	31.5	0	58	11	47	48	-1	84	85	49	48.9
071025data3	31.5	2.5	58	11	12.4	84	-71.6	62.6	63.8	42.9	42.3
071030data1	31.5	3	58	4	22.8	74.3	-51.5	82.6	82.4	56.2	55.7
071030data2	31.5	2.5	58	4	17.6	77.9	-60.3	77.2	76.2	56	55
071031data1	31.5	3	58	12	31.5	65.8	-34.3	90.6	92.6	67.6	66.7
071101data1	31.5	3	58	8	1.4	96.9	-95.5	13.2	15.1	–	–
071102data1	31.5	3	58	14	6.3	93.5	-87.2	34.6	36.7	31.1	31.4
071102data2	31.5	2.5	58	14	5.3	92.9	-87.6	27.9	28.2	30	30.8
071102data3	31.5	3	58	15	27.7	66.7	-39	89.6	87.8	64.1	62.3
071105data1	31.5	3	58	11	11.3	84.7	-73.4	59.3	60.3	41.5	41.1
071105data2	31.5	2.75	58	11	9.6	87	-77.4	56.7	57.1	41.4	40.9
071105data3	31.5	2.5	58	11	9.2	88.5	-79.3	53.3	54.2	41.5	41
071106data1	31.5	2.25	58	11	8.1	87.5	-79.4	44.6	45	42.9	41.5
071106data2	31.5	2	58	11	14.8	82.4	-67.6	45.7	45.9	42.5	41.5
071106data3	31.5	1.75	58	11	20.8	76.5	-55.7	42.5	43.1	42.7	42.5
071106data4	31.5	1.5	58	11	31.3	65.9	-34.6	46.7	46.5	43.5	43.2
071106data5	31.5	1.25	58	11	43.9	52.8	-8.9	62.5	63.2	44.5	44.2
071106data6	31.5	1	58	11	47.5	49.6	-2.1	74.7	74.7	45.8	45.9
071126data1	31.5	4	58	11	11	87	-76	47.5	47.6	40.3	40
071126data2	31.5	5	58	11	43.6	53.5	-9.9	66	68	43	43

References

[1] C. Brukner and A. Zeilinger, Phil. Trans. R. Soc. Lond. **360**, 1794 (2002).

[2] G. Jaeger, A. Shimony, L.Vaidman, Phys. Rev. A **51**, 54 (1995).

[3] C.K. Hong and T.G. Noh, J. Opt. Soc. Am. B **15**, 1192 (1998).

[4] A. F. Abouraddy, M.B. Nasr, B.E.A. Saleh, A.V. Sergienko and M.C. Teich, Phys Rev A **63**, 063802 (2001).

[5] E.J.S. Fonseca, C.H. Monken, S. Pádua and G.A. Barbosa, Phys. Rev. A **59**, 1608 (1999).

[6] C.H. Monken, P.H.S. Riberio, S. Pádua, Phys. Rev. A **57**, 3123 (1998).

[7] M.H. Rubin, Phys. Rev. A **54**, 5359 (1996).

[8] L. Mandel and E. Wolf, *Optical Coherence and Quantum Optics* Cambridge, University Press (1995).